Ni/C nanostructures: Impregnating-method preparation, textural and structural features, and catalytic property for the hydrogen production

Félix Galindo-Hernández[a)]
Universidad Nacional Autónoma de México (U.N.A.M.), 01000 México City, México; ESIQIE, Instituto Politécnico Nacional, 07738 México D. F., México; and Department of Chemistry, Universidad Autónoma Metropolitana-Iztapalapa, Mexico City, D.F. 09340, México

Jin-An Wang and Lifang Chen
ESIQIE, Instituto Politécnico Nacional, 07738 México D. F., México

Xim Bokhimi
Universidad Nacional Autónoma de México (U.N.A.M.), 01000 México City, México

Alejandro Pérez-Larios and Ricardo Gómez
Department of Chemistry, Universidad Autónoma Metropolitana-Iztapalapa, Mexico City, D.F. 09340, México

A series of Ni/C catalysts with different Ni content (15, 20, and 30 wt% Ni) were prepared by the wet incipient impregnation method. Their textural properties were studied by surface fractal dimension (D_s) and nonlocal density functional theory using nitrogen sorption data. Their structural properties were studied by x-ray diffraction, Rietveld refinement, radial distribution functions (RDFs), and electron density maps of Fourier. Surface areas of Ni/C catalysts decreases slightly from 614 to 533 m^2/g as Ni content increases from 15 to 30 wt%; however, the Ni crystallite size (5.1–31.4 nm) increases as the nickel content increases. Many point defects were found by Rietveld refinement in nickel nanostructures of Ni/C catalysts with 20 and 30 wt% Ni. This was confirmed by RDFs and electronic density maps. On the other hand, the hydrogen production via the photodehydrogenation of ethanol is very sensitive to the nickel crystallite size and the number Ni atoms in nickel nanostructures. The maximum reaction rate (363.64 µmol/h) is achieved on Ni/C catalyst with 15 Wt% Ni content which has the smallest crystallite size (5.1 nm) and less point defects in its nickel nanostructures. Ab initio calculations were performed to propose a reaction mechanism in the photodehydrogenation of ethanol.

I. INTRODUCTION

Many investigations of new materials with catalytic properties have been focused on the hydrogen production by means of water, methane, methanol, and ethanol among others as hydrogen precursors.[1–7] A number of Ni-based catalysts with different supports, for example, Ni/CeO$_2$–ZrO$_2$,[1] Ni/CeO$_2$,[2] Ni/γ-Al$_2$O$_3$,[3] Ni–Cu–Fe/γ-Al$_2$O$_3$,[4] Cu–Ni/SiO$_2$,[5] Ni/SiO$_2$,[6] and Ni/ZnO[7] have been successfully applied in the hydrogen production. Nickel is chosen and widely used as the active phase in steam-reforming reactions because of its high activity and low cost. However, the nanostructural properties of Ni supported on activated carbon in the hydrogen production have not been extensively studied.

For this, in the present research work, a series of Ni/C catalysts with various nickel loadings were prepared by

the wet incipient impregnation method using nickel nitrate as the nickel precursor and activated carbon as the support. In oxidative dehydrogenation reactions at 623 K, Pereira et al.[8] reported catalytic photoactivity of carbon. In this research, the photodehydrogenation of ethanol is performed under mild conditions (pH $\approx$ 7, 298 K). Although nickel immobilized on activated carbon is responsible for the photodehydrogenation of ethanol, the textural properties of carbon allow us to improve reaction kinetics.

The textural properties were studied by surface fractal dimension (Ds) and nonlocal density functional theory (NLDFT) using adsorption–desorption isotherms data. The crystalline structure and the point defects in Ni crystallites were studied by x-ray diffraction (XRD), Rietveld refinement, radial distribution functions (RDFs), and electron density maps of Fourier. Morphology of the Ni/C catalysts was studied by transmission electron microscopy (TEM). The catalytic activity of the catalysts was evaluated in the photodehydrogenation of ethanol.[9] According to ab initio calculations [DFT/generalized gradient approximation (GGA)/Perdew–Burke–Enzerhof (PBE)] performed

---

for this paper, the ethanol–water solution can be dehydrogenated using Ni/C photocatalysts.

The discussion of results was focused to show that hydrogen production is sensitive to the nanostructures of the Ni/C catalysts.

II. EXPERIMENTAL

A. Catalysts preparation

The Ni/C catalysts were prepared as follows: a calculated amount of nickel nitrate $Ni(NO_3)_2 \cdot 6H_2O$ (Sigma-Aldrich, St. Louis, MO) was respectively added into 3 beakers containing 10-mL water to obtain 15, 20, and 30 wt% nickel on carbon. Next, carbon (CARBOCHEM, Ardmore, PA, 900 m^2/g) was added to nickel solutions with constant stirring for 5 min. Afterward, the solids were dried at 373 K for 24 h. The dried NiO/C solids were annealed in nitrogen flow at 773 K for 4 h. Finally, the NiO/C solids were reduced in H_2 flow (150 mL/min) at 773 K for 3 h to obtain Ni/C catalysts.

B. Characterization

1. Adsorption measurements

N_2 sorption isotherms at 76 K on Ni/C were determined by means of an automatic Quantachrome Autosorb 3B instrument (Boynton Beach, FL). Prior to the adsorption run, all samples were outgassed overnight at 573 K. N_2 and He gases required for the operation of the sorption apparatus were UHP grade. The specific surface areas were calculated from desorption isotherms by using the BET equation, and the pore size distribution functions (PSDFs) were obtained by NLDFT using a slit pore model.[10]

The NLDFT method for pore size analysis is considered to be one of the most advanced methods with regard to pore size analysis of micro- and mesoporous materials. In this technique, a set of isotherms was calculated for a set of pore sizes in a given range.[11,12] Such a set of isotherms, called kernel, is the basis for pore size analysis by density functional theory (DFT). The calculation of the pore size distribution is based on a solution of the generalized adsorption isotherm equation (GAI), which correlates the kernel of theoretical adsorption/desorption isotherms with the experimental sorption isotherm:

$$N(P/P^0) = \int_{W_{\text{MIN}}}^{W_{\text{MAX}}} N(P/P^0, W)f(W)\mathrm{d}W \quad ,$$

where $N(P/P^0)$ are the experimental adsorption isotherm data, W is the pore width, $N(P/P^0,W)$ is the isotherm on a single pore of W, and $f(W)$ is the PSDF. The GAI equation reflects the assumption that the total isotherms consist of a number of individual "single pore" isotherms multiplied by their relative distribution, $f(W)$, over a range of pore sizes. Hence, NLDFT allows the adsorption study over a complete range, and it is possible to obtain with a single

method a pore size distribution which extends over the complete micro–mesopore range. In this work, we have preferred the NLDFT model approach to evaluate PSDF since this method eliminates some of the most important shortcomings inherent to the BJH analysis[13,14] mainly because it takes into account the variety of interaction potentials (i.e., solid–adsorbate, adsorbate–adsorbate, etc.) existing in the adsorption system and also because it can shed light about some of the particularities of the mechanistic aspects of the evaporation and condensation processes that are taking place inside the cavities and throats.[15]

2. Fractal dimension

The fractal dimension is a measure of classifying and quantitatively comparing complex chaotic patterns as shown in solid surfaces. In this way, it has been shown that although a chaotic behavior is essentially unpredictable in detail, this can be modeled quantitatively in a statistical sense. In the present work, the values of fractal dimension D_s were calculated from the adsorption–desorption isotherms data using the Frenkel–Halsey–Hill equation expressed as follows[16,17]:

$$Ln(S^{\text{lg}}) = \text{const} - (3 - D_s)Ln(\mu) \quad ,$$

where S^{lg} is the amount adsorbed at the relative pressure P/P^0 at the absolute temperature T and μ is the so-called adsorption potential defined as

$$\mu = RTLn\left(\frac{P^0}{P}\right) \quad .$$

3. Molecular hardness and UV-vis diffuse reflectance spectroscopy

The molecular hardness (η) is a global property which allows us to measure the resistance imposed by a system to charge transfer.[18–21] In other words, less reactive systems have the highest hardness in agreement with the maximum hardness principle.[21] The molecular hardness is defined by the derivate of energy, which is expressed in terms of the number of electrons N and external potential $v(r)$:

$$\eta = \frac{1}{2}\left[\frac{\partial^2 E}{\partial N^2}\right]_{v(r)} \quad ,$$

where the band gap energy (E_g) can be expressed as follows:

$$E_g = \left[\frac{\partial^2 E}{\partial N^2}\right]_{v(r)} \quad .$$

Experimentally the molecular harness of powder semiconductors can be obtained by the Kubelka–Munk's equation applied to UV-vis diffuse reflectance data as follows[22]:

$$[F(R_\infty)h\nu]^2 = C_2(h\nu - 2\eta) \quad ,$$

where $R_\infty = R_{sample}/R_{standard}$, C_2 is the constant of proportionality and $h\nu$ is the photon energy. For this purpose, UV-vis spectra were obtained with a Varian Cary III UV-vis spectrophotometer (Cary, NC) coupled with an integration sphere for diffuse reflectance spectroscopy. A sample of MgO with a 100% reflectance was used as a reference.

4. XRD and Rietveld refinement

XRD data were obtained in a Bruker Advance D-8 diffractometer (Madison, WI) with Cu K$_\alpha$ radiation equipped with a detector Lynxeye and a graphite secondary beam monochromator. Intensities were obtained in the 2θ range between 40 and 110° with a step of 0.01° and a measuring time of 10 s per point. The nickel structures were refined by the Rietveld method with the parameters shown in Table I.

With the purpose of knowing quantitatively changes in densities obtained by the Rietveld method, the theoretical density (Table I) for a nickel structure was calculated by the following equation:

$$\rho_{Ni} = \frac{(Z)(MM_{Ni})(\text{Avogadro's number})^{-1}}{\text{Cell volume}} \quad ,$$

where MM_{Ni} is the atomic weight and Z is the number of nickel atoms per cell. The "number of nickel atoms" per unit cell was calculated taking into account a face-centered cubic (FCC) structure as that shown in Fig. 1 and the following equation[23]:

$$Z = \frac{6}{2}(\text{face}) + 8 * \frac{1}{8}(\text{vertexes}) = 4\frac{\text{atoms}}{\text{cell}} \quad .$$

Finally, the theoretical occupancy for Ni was calculated using its multiplicity and the maximum multiplicity for its space group as follows:

$$\text{Occupancy theoretical} = \frac{\text{Multiplicity of Ni}}{\text{Maximum multiplicity}}$$
$$= \frac{4}{192} = 0.02083 \quad .$$

This value means that 4 nickel atoms distributed, as that shown in Fig. 1, corresponding to an occupancy value of 0.02083.

5. Electron density maps of Fourier

Electron density maps are a bidimensional description of the electron density in a crystal structure, i.e., these maps describe content and the structural disorder (if any) in crystallites. The electronic density maps for Ni/C catalysts were obtained from XRD data on a point (x, y, z) of the crystallite cell with volume V and calculated by Fourier's series[24] using the structural factors $F(h, k, l)$:

$$\rho(x,y,z) = V^{-1}\sum_h\sum_k\sum_l F(h,k,l)$$
$$\times \exp[-2\pi i(hx + ky + lz)] \quad ,$$

where (x, y, z) represent a vector r of real space, with one vectorial space (a, b, c), and (h, k, l) coordinates of one vector from the reciprocal space with base $(a*, b*, c*)$, i.e., they are the coordinates from the diffraction plane that it is given by the Bragg's Law. The electron density distributions were delineated for a slice with $z = 0$, i.e., face ba. In this work, the electron density maps are focused to look for changes between the interatomic distances of nickel atoms.

6. Radial distribution functions

RDF, or the pair correlation function $[G(r)]$, is a measure to determine the correlation between particles within a system. Specifically, it is the probability of finding a particle at a distance of r away from a given reference particle. RDFs $G(r)$ of Ni/C catalysts calcined at 773 K were obtained with a Siemens D500 diffractometer (Cherry Hill, NJ) coupled to a molybdenum anode x-ray tube. Intensities and angles were measured with a step of 0.01°, from 2 to 110°, and these were the input data for the program Radiale.[25] RDFs were obtained up to a radius of 6 Å.

TABLE I. Parameters utilized for nickel structure refinement.

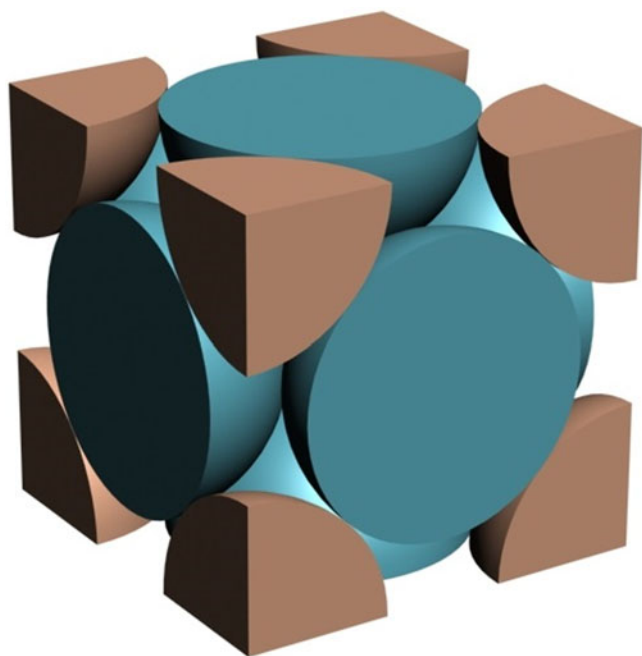| | | | | Nickel (FCC) | | | | | | | | | |
				Atomic fractional coordinates			Lattice parameters			Angles			
Atom	Space group	Site	Occupancy	x	y	z	a (Å)	b (Å)	c (Å)	α (°)	β (°)	γ (°)	Density (g/cm^3)
Ni	$Fm3m$	4a	0.02083	0.000	0.000	0.000	3.5238	3.5238	3.5238	90	90	90	8.902

FIG. 1. Hypothetical chemical species (identical) in a unit cell: FCC.

7. Transmission electron microscopy

TEM analyses of Ni/C crystallites were performed in a JEE-2200FS transmission electron microscope (JEOL USA, Inc., Peabody, MA) with an accelerating voltage of 200 kV. The microscope is equipped with a Schottky-type field emission gun and an in-column omega-type energy filter.

8. Ab initio calculations using DFT

For ethanol–water system, interaction energy (ΔE), electronegativity (χ), molecular hardness (η), and energy band gap (E_g) were calculated using a molecular mechanics program (Accelrys Materials Studio V6.1).[26] Interfacial binding characteristics of ethanol and their interactions with water were investigated using molecular mechanics. A representative structure of ethanol and water were utilized for the calculations.

The calculations are performed within the DFT through the GGA with the PBE functional[27] by using norm conserving pseudopotentials.[28]

9. Catalytic activity measurement

Photoactivity of the Ni/C catalysts was evaluated using a 200-mL Pyrex batch reactor containing an aqueous ethanol–water solution with a molar ratio of 1:1 and 0.2 g of catalysts. Photoirradiation was made using a high-pressure Hg lamp encapsulated in a quartz tube with $\lambda = 254$ nm (4.88 eV) and an intensity of 4.4 mW. Circulation of gases was made with a peristaltic pump. The reaction

procedure was followed by taking sample each hour. Products were analyzed using gas chromatography in a GC Varian 3800 with a detector TCD and capillary column (Mol Sieve 5A).

III. RESULTS AND DISCUSSION

A. Textural properties

Figure 2 displays the Frenkel–Halsey–Hill fractal analysis of the adsorption–desorption isotherms of the Ni/C catalysts annealed at 773 K, and Fig. 3 shows their loops of adsorption–desorption isotherms. The specific surface areas of the Ni/C samples are reported in Table II. It can be seen that the addition of nickel on carbon decreases slightly the BET specific surface area, from 614 m^2/g for the sample 15 wt% Ni/C to 533 m^2/g for the sample 30 wt% Ni/C. These results suggest that the intrawall pores and principal channels or micropores of these samples are blocked by nickel deposits, which are also supported by the facts that the values of intrawall volume diminished from 215 to 154 mm^3/g and the micropore volume diminished from 190 to 141 mm^3/g as the Ni loadings increased from 15 to 30 wt%.

By comparing Tables II and III, we may suggest that an important fraction of the surface areas reported in Table II is the contact area between N_2 and Ni crystals. We can note that the sample with the lowest nickel content shows the smallest crystallite size, and the sample with the highest nickel content shows the biggest crystallite size; nevertheless, there are not remarkable differences among the values of the surface areas. Therefore, the facts mentioned above allow us to infer that between the exposed surface area of Ni crystallites and the crystallite sizes, there is an approximately constant ratio (in the range of 15–30 wt% Ni).

On the other hand, the calculated average value of the fractal dimension is 2.9, which seems to be too high because the regular values of fractal dimension should be between 2.0 and 3.0. This result indicates that the surfaces of the Ni/C materials are too rough. These results are characteristic of materials with high porosity and/or microporosity. Therefore, the Ni/C materials possess high capacity of adsorption, and hence, their D_s values are less sensitive to high nickel contents. Figure 4 shows PSDFs for the samples with 15, 20, and 30% of nickel deposits. These materials have a bimodal pores system (1.96 and 4.74 nm of diameter); however, the profiles of pore diameter distribution were not significantly varied with the nickel content. These data are in good agreement with the D_s values reported above.

B. UV-vis absorption spectra

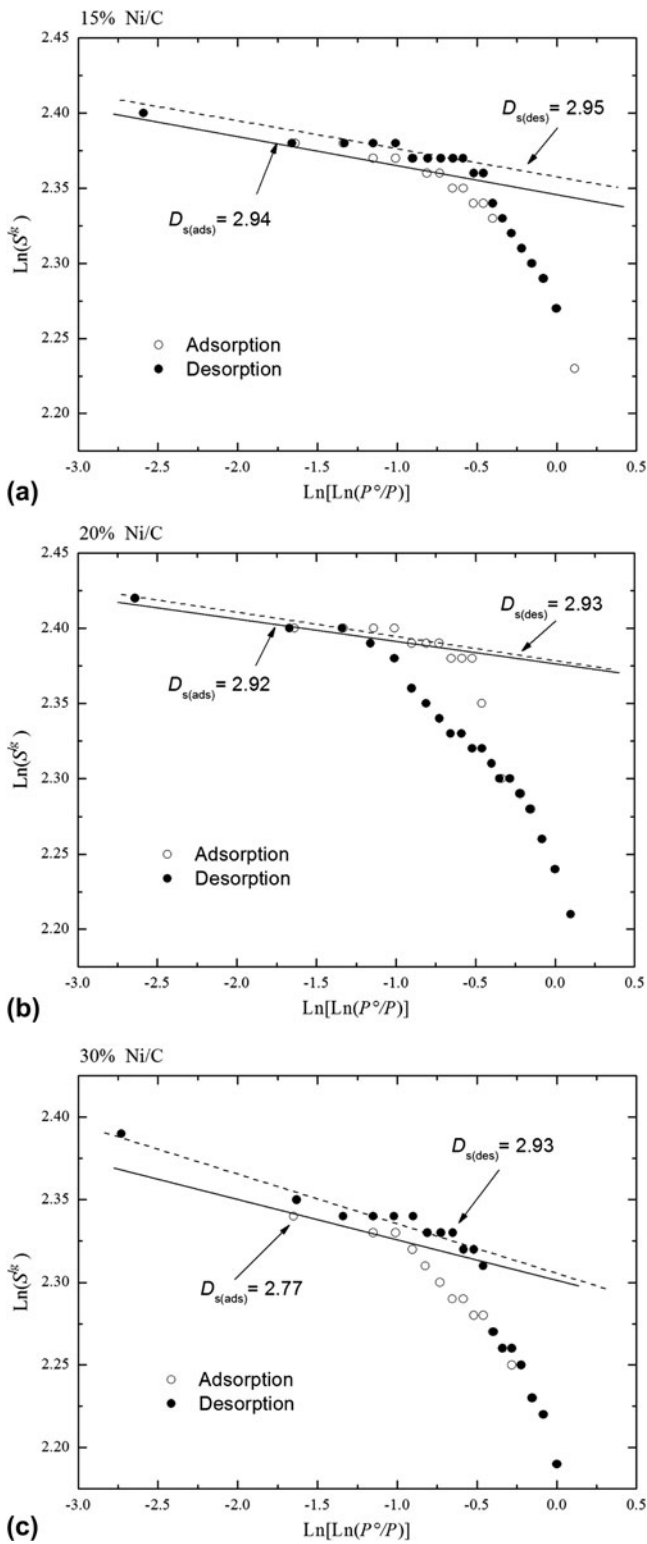UV diffuse adsorption spectra for Ni/C catalysts as a function of the nickel content are displayed in Fig. 5.

FIG. 2. Frenkel–Halsey–Hill fractal analysis of the adsorption–desorption isotherms of Ni/C catalysts as a function of the Ni content. (a) 15 wt% Ni, (b) 20 wt% Ni, and (c) 30 wt% Ni.
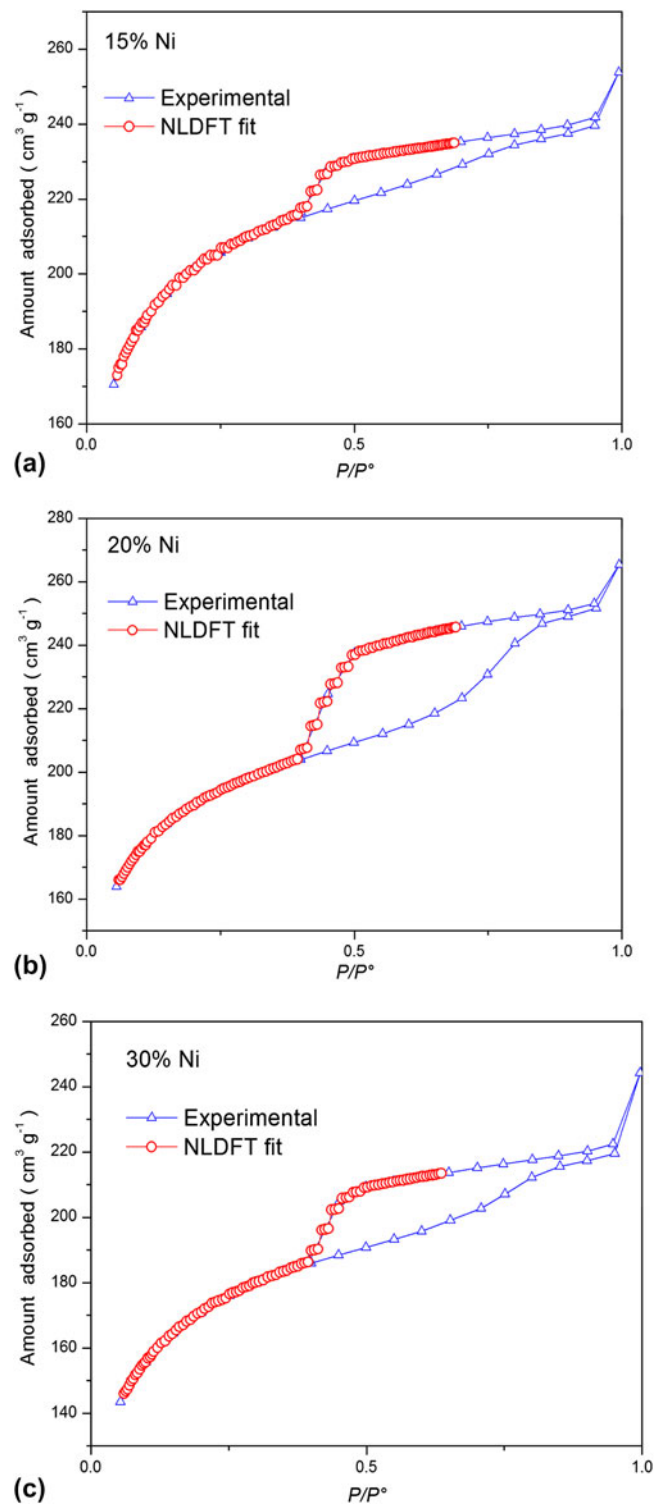

FIG. 3. Comparison of the experimental nitrogen desorption isotherm on Ni/C catalysts with the NLDFT isotherm in a slit pore as a function of the Ni content. (a) 15 wt% Ni, (b) 20 wt% Ni, and (c) 30 wt% Ni.

Zhang et al.[29] reported that the wave length of the absorption band for nickel surface plasmon is a function of the particle size. Plasmons are collective oscillations of the free electron gas density at optical frequencies. The plasmons can couple with a photon to create another quasiparticle.[30] Taking into account the mentioned above, the possibility of finding surface plasmons that resemble those arising from

TABLE II. Pore structure parameters for Ni/C catalysts.

Substrate	S_{BET} (m^2/g)	S^{NLDFT} (m^2/g)	V_P^{NLDFT} (mm^3/g)	D_P^{NLDFT} (nm)	V_{iw}^{NLDFT} (mm^3/g)	V_{Mi} (mm^3/g)	D_s
15% Ni/C	614	670	352 (50)	1.96 (0.20)/4.74 (0.38)	215	190	2.95
20% Ni/C	581	632	350 (40)	1.96 (0.22)/4.74 (0.44)	181	180	2.95
30% Ni/C	533	559	304 (40)	1.96 (0.20)/4.74 (0.44)	154	141	2.93

S_{BET} was calculated using the molecular cross-sectional area of N$_2$, 0.162 nm^2 per molecule.
S^{NLDFT} was obtained by the NLDFT from the desorption branch.
V_P^{NLDFT}: total pore volume; D_P^{NLDFT}: pore diameter taken from the maximum of the PSD curve. For samples with bi-modal PSDs, two values are given; V_{iw}^{NLDFT}: volume of the intrawall; V_{Mi}: micropore volume determined by the t-method; Ds: surface fractal dimension.
The numbers in parentheses correspond to the standard deviation.

NiO structures within the induction period may not be discarded. However, NiO crystals formed at the end of the reaction is not feasible because Comerta and Pratt[31] have reported that the standard molar Gibbs free energy of formation of NiO is within the temperature range 760–1275 K. In this paper, the photodehydrogenation of ethanol is carried out under mild conditions of temperature and pH (298 K and pH ≈ 7).

The maximum of the surface plasmon resonance is around 318, 326, and 346 nm, corresponding to deposits of 15, 20, and 30 wt% Ni, respectively. Moreover, Table III shows nickel particle sizes of 5.1, 19.7, and 31.4 nm for 15, 20, and 30 wt% Ni content, respectively. Thus, a particle size effect on Ni surface plasmon resonance can be clearly observed. When Ni content increases, the width of the absorption spectra increases, similar to the results reported by Zhang et al.[29] This correlation shows that the surface plasmon resonance of metallic Ni nanoparticles is sensitive to the particle size.

C. XRD and Rietveld refinement

Figure 6 displays XRD patterns and Rietveld fits for the Ni/C materials. Five peaks corresponding to Bragg reflection planes of nickel crystallites were observed. Figure 7 shows the TEM image of catalysts containing 30 wt% Ni. Ni particle diameter ranges are within 5 and 30 nm, most of them are between 20 and 30 nm. TEM observations agree with Rietveld refinement results reported in Table III. There are many Ni atoms close to each other, so that their valence orbitals overlap producing a larger metallic network. This fact is justified by the band model of the metal-binding theory.

Important differences related to the symmetry properties (occupancy values) in the nickel nanostructures in the three Ni/C materials under study were found. The occupancy values are reported in Table IV. Differences between occupancies mean point defects in nickel crystallites, i.e., nickel deficiencies and/or vacancies in its lattice. It must be noted that if the nickel vacancies were produced by displacing some lattice atoms, the atoms released are either trapped within the lattice or are moved out to the surface to form new crystal layers (Schottky defect).[32] Otherwise, if nickel

TABLE III. Rietveld refinement data and photoactivity of the Ni/C catalysts.

Sample	Crystallite size (nm)	Lattice parameter a (nm)	Density (g/cm^3)
15% Ni/C	5.1 (0.3)	0.35286 (3.3)	8.891
20% Ni/C	19.7 (0.2)	0.35266 (1.1)	5.405
30% Ni/C	31.4 (0.3)	0.35264 (0.8)	5.807

The numbers in parentheses correspond to the standard deviation.

atoms were not confined to the nearest-neighbor shell of nickel atoms, the disturbance could perturb several lattice sites. The point defects can be Frenkel or Schottky. A Frenkel defect is when the displaced nickel atom is retained in the interior of the crystal at an interstitial site. In many cases, the vacancy–interstitial Frenkel pair is well separated, and the annealing stage may lead to alternative reaction with other interstitials, impurity atoms, or extended defects. It should be noted that as a consequence of the vacancies formed, new interstitial structures and more complexes can be developed. The three simplest interstitial sites are: at the interstices of normal lattice sites, as a pair of nickel atoms sharing a single lattice site, and as an additional nickel atom inserted into a row of atoms.[32,33] The samples with 20 and 30 wt% Ni content, their occupancy values are very similar to each other (Table IV) and could mean that some atoms are out of their regular positions in the nickel structures, and hence, these could be forming Frenkel defects.[32] It is important to note that vacancies of nickel do not mean empty sites in the nickel lattice because these vacancies could be occupied by other atoms. In this case, it could be C atoms.

Other related differences now with the lattice parameter a in the nickel nanostructures in the three Ni/C materials were found. The refined lattice parameter a is different within the three samples under study (see Table III). This can be a consequence of point defects in Ni nanostructures. Something from this was already discussed above. To explain this, we will advance two hypotheses that will be justified after discussing RDF results: (i) observing Table III and reflection picks in Fig. 6, the point defects may be localized on the perimeter refection plane (111);
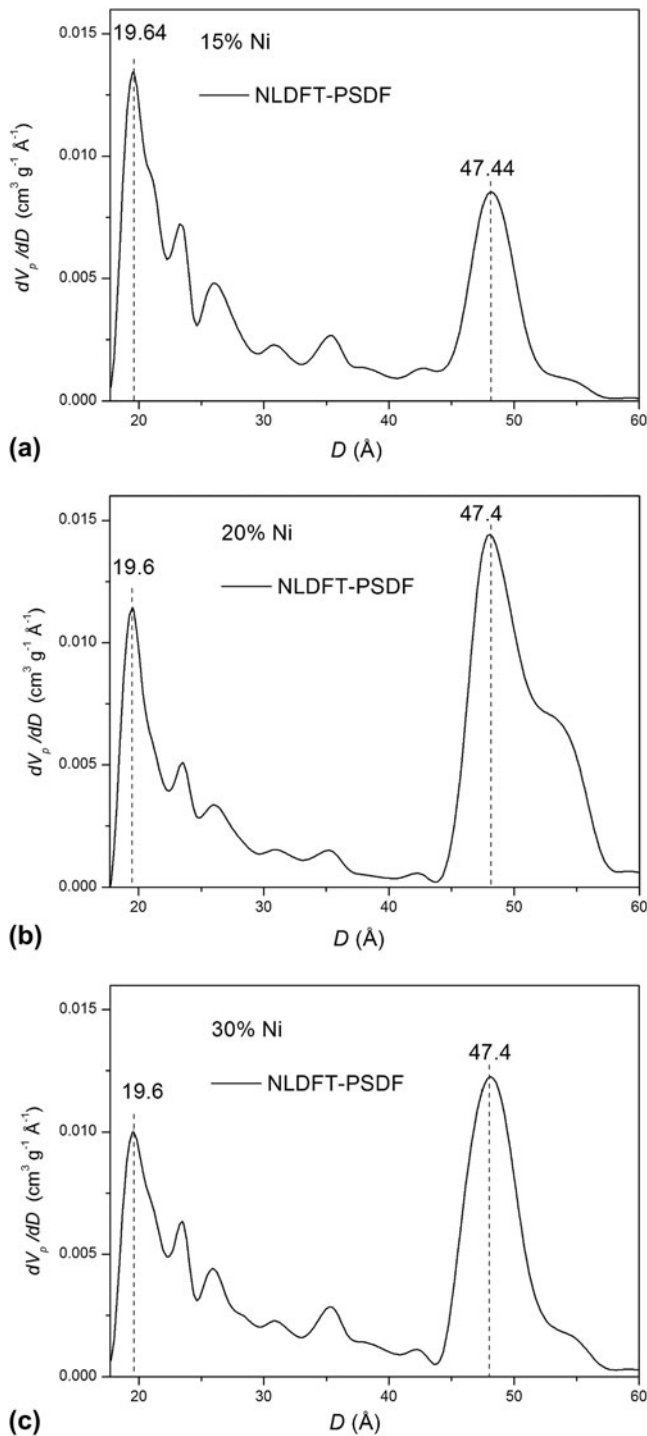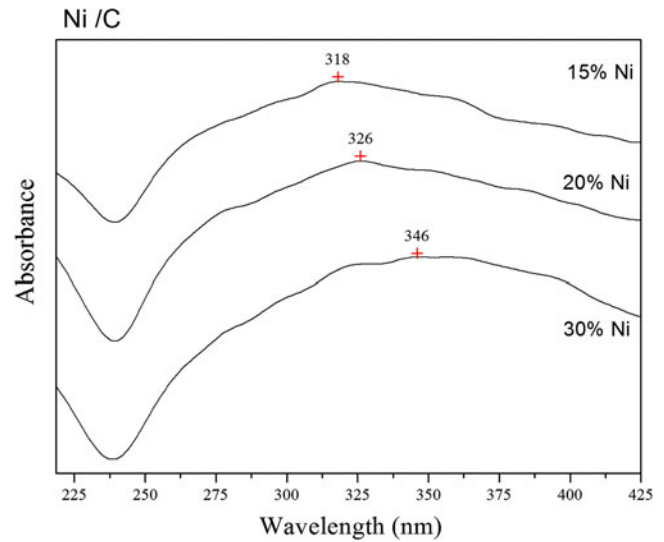
(a)

Ni /C

FIG. 5. UV-vis spectra for Ni/C catalysts.

$$\text{Reflection plane area} = a^2\sqrt{2} \quad .$$

From the last equation, the results reported in Table III and Fig. 8, we can suggest the possible displacement of Ni atoms along of the perimeter of the reflection plane (111). Moreover, Johnson[34] considers six possible configurations for atoms occluded interstitially in a FCC lattice such as (A) octahedral, (B) tetrahedral, (C) crowdion, (D) (100) split, (E) (111) split, and (F) (110) split. These configurations can also generate point defects by changes in positions of nickel atoms in nickel structures.

(b)

D. Radial distribution function

RDFs obtained from XRD for Ni/C materials at different nickel contents are displayed in Fig. 9. Each interatomic distance localized by XRD between two Ni atoms contained within the nickel structures is being represented by one peak in one RDF. Hence, all peaks in each RDF are all possible interatomic distances between the Ni atoms included into the nickel structures of each Ni/C sample under study. Theoretical distances between Ni atoms for a unit cell without point defects are reported in Table V.

Comparing picks of the interatomic distances taken from RDFs and theoretical values with each other (see Fig. 9 and Table V), absence of peaks corresponding to first neighbors (3.5 Å) in samples prepared at 20 and 30 wt% Ni was the first thing noticed. Taking into account the Ni structures displayed in Fig. 8 and the missing peaks, we could suggest point defects in the midpoints of the line segments of the perimeter of the plane of reflection (111).

(c)

FIG. 4. Pore size distribution of Ni/C catalysts as a function of the Ni content, calculated from the NLDFT model using desorption isotherms. (a) 15 wt% Ni, (b) 20 wt% Ni, and (c) 30 wt% Ni.

(ii) additionally, changes in the lattice parameter a shown in Table III can be due to displacements of some nickel atoms onto the lattice surface (Schottky defect).

Considering that the unit cell FCC has dimensions $a = b = c$, the reflection plane area (111) will be related with a as follows:

Regarding second neighbors, the interatomic distances shown in Fig. 9 and Table V for samples prepared at 15 and 20 wt% Ni are higher than theoretical values, which could correspond to the vertexes of the reflection plane
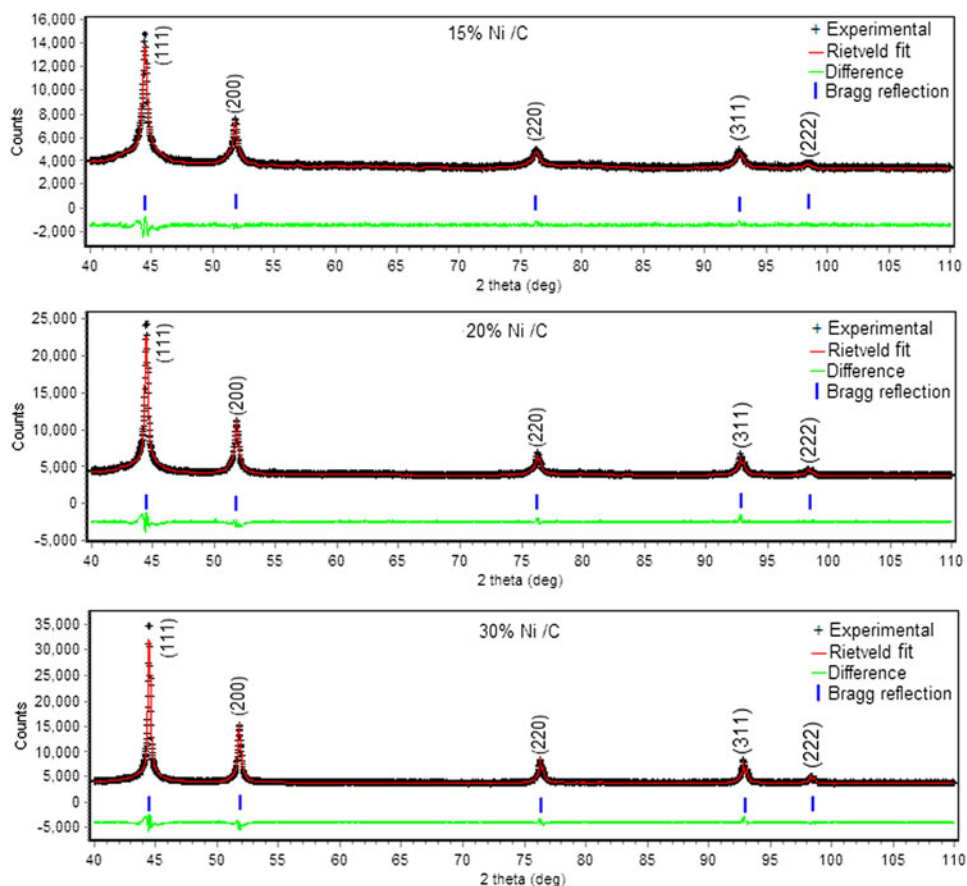
FIG. 6. Rietveld plot of the Ni/C catalysts (weighted profile R-factor, Rwp = 2.8, 2.2, and 2.3 for 15, 20, and 30 wt% Ni respectively). In the upper curve crosses correspond to the experimental data and the continuous line corresponds to those calculated; the lower curve is the difference of both data. The tick marks correspond to nickel structure according is indicated in the figure. The numbers in parenthesis corresponds to different reflection planes (*hkl*) of the crystalline structures.

(111) at shown in Fig. 8, and this could be either associated Frenkel or Schottky defects. For the sample prepared with 30 wt% Ni, the distance between the second neighbors is absent. Elsewhere, using the refined lattice parameter *a* (Table III) and also considering the reflection plane area equation, we can deduce that the reflection plane areas (111) are in the following order:

$$S_{(111)}^{15wt\%Ni} > S_{(111)}^{20wt\%Ni} > S_{(111)}^{30wt\%Ni} \quad .$$

This result implies that the sample prepared at 15 wt% Ni must have the biggest surface area measured by N_2 sorption. Table II shows the following order:

$$S_{BET}^{15wt\%Ni} > S_{BET}^{20wt\%Ni} > S_{BET}^{30wt\%Ni} \quad .$$

Hence, the reflection plane areas measured by Rietveld refinement and surface areas measured by N_2 sorption agree each other, and at the same time, these agree with the RDF results.

After comparing the crystallite sizes and occupancies reported in Tables III and IV, one can note that if the
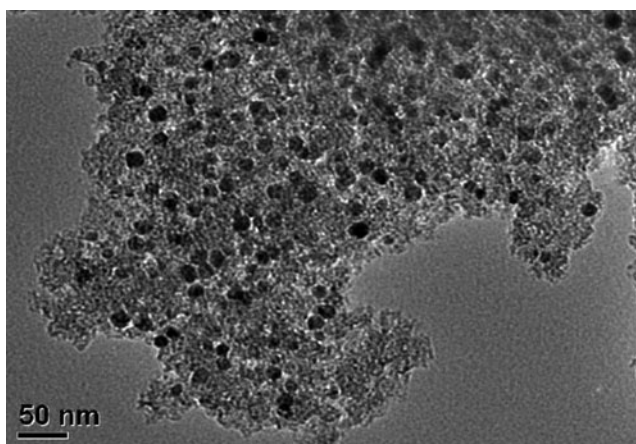

FIG. 7. TEM image of catalysts containing 30 wt% Ni.

crystallite size decreases, the occupancy values increase as a function of the Ni content. In view that the crystallite sizes for 15 wt% Ni are smaller than other contents, it appears that the Ni atoms are more ordered in these nickel nanostructures.

Therefore, the nickel content plays an important role in the generation of point defects, and at higher nickel nitrate content, there is a greater probability to obtain a greater amount of nickel particles forming agglomerations during the thermal treatment.

E. Electron density maps of Fourier

The metal nickel atoms have few electrons in its last layer, and then they can easily lose these electrons and become positive ions. The positive ions are arranged in space forming a metal network and the valence electrons detached from atoms form a cloud of electrons that can move across the network. Thus, the whole of the positive ions of the metal is attached through the cloud electrons that are surrounding them. This fact can be seen by electron density maps obtained from XRD data. In the base plane (face *ab* normalized to 1), the electron density distributions around the nickel structure of the Ni/C catalysts are shown in

TABLE IV. E_g, η, occupancies and photoactivity of the Ni/C catalysts.

Sample	E_g (eV)	η (eV)	*O_{Ni}	[Ni]	k (μmol/h)
Photolysis	...	...	...	...	79.00
15% Ni/C	4.13	2.05	0.021	14.0	363.64
20% Ni/C	4.13	2.05	0.013	8.7	296.00
30% Ni/C	4.00	2.00	0.014	9.4	286.40

E_g: band gap energy; η: molecular hardness; *refined occupancies; [Ni]: whole nickel atoms per unit cell. These Ni atoms correspond to the refined occupancies O_{Ni}; k: kinetic constant.
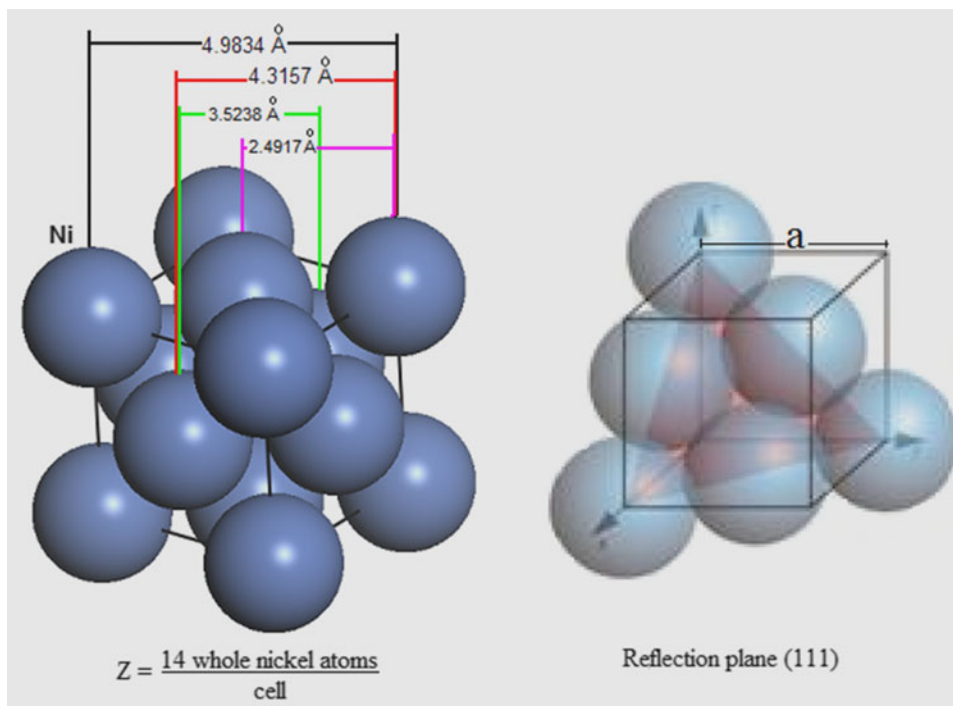
Fig. 10. The number of contours in the electron density maps gives the relative electron concentration. In Fig. 10, the valleys are represented by few contour lines that at the same time represent distances between the central atom and the atoms placed in the vertexes of nickel lattice (see also Fig. 8).[32,35] Differences among the contours of the valleys shown in Fig. 10 are shifts of distances between the nickel atom neighbors as a function of the nickel content. As compared with the results obtained from RDFs (Fig. 9), we may conclude that the amount of nickel deposited on carbon greatly influences the structural properties of Ni/C catalysts.

F. Catalytic activity

The activities of the Ni/C catalysts were evaluated in the hydrogen production from ethanol photodecomposition at room temperature. The evolution of the hydrogen produced as a function of time is shown in Fig. 11. From the data of the curves, the apparent rate constant k was calculated by the differential method for an irreversible unimolecular-type zero-order reaction[36]:

$$-r_A = -\frac{dC_A}{dt} = k \quad ,$$

where C_A is the concentration at time t, and k is the constant kinetic.

An acceptable linearity was obtained for 6 h of reaction by applying the zero-order kinetic equation (Fig. 12). The values calculated from selected slopes are reported in

FIG. 8. Nickel crystal lattice: FCC with a = 3.5238 Å, ρ = 8.902 g/cm³ and Wyckoff site: 4a (*Fm3m*). The theoretical distances correspond to a nickel structure without point defects.

Table IV. A maximum constant rate, $k = 363$ μmol/h, was obtained for the sample with 15 wt% Ni. Regarding CO gas, it was also measured, however, at the end of 10 h, the concentration of CO gas was less than 90 μmol. Then, we decided not to report it.

1. Photoactivity versus structural properties

The nickel crystallite sizes calculated by Rietveld refinement (Table III) were plotted as a function of the nickel content and compared with the catalytic activity (Fig. 13), where the maximum activity was achieved by 15% Ni/C catalyst, which has the smallest crystallite size among the three Ni/C catalysts.

To understand these last results and their relationship with the structural properties of the Ni/C catalysts, the whole atoms corresponding to the refined occupancies (compare Figs. 1 and 8) were calculated. These were displayed with the catalytic activity as a function of the nickel content in Fig. 14.

The results shown in Figs. 13 and 14 confirm that the crystallite size of nickel nanoparticles and the number of

whole nickel atoms per unit cell in Ni nanostructures are the main factors affecting the catalytic activity.

On the one hand, both the band gap energy and the molecular hardness values shown in Table IV are the same for all the samples. That is, the resistance to charge transfer is the same for all samples under study. It appears that kinetic constants depend on occupancy values as it was pointed out before.

2. Photodehydrogenation of ethanol/water solution using Ni/C catalysts

The global molecular properties (ΔE, χ, η, and E_g) for ethanol–water and ethanol–ethanol systems were obtained by theoretical calculations (DFT/GGA/PBE) and are reported in Table VI. We can note the following: (i) ethanol molecules and water are less close to each other, (ii) for the ethanol–water system, the tendency to attract electrons to itself is larger than the ethanol–ethanol system, (iii) given that the ethanol–water system has the bigger molecular hardness, this is less reactive than the ethanol–ethanol system, and (iv) water which is used as a solvent increases the band gap energies of all systems.

The photodehydrogenation of ethanol starts with the nucleophilic attack from Ni/C catalysts to hydrogen (site 9) and was determined by theoretical calculations DFT/GGA/PBE as reported in Table VII.

By comparing Tables IV, VI, and VII with each other, we can conclude that the light intensity of 254 nm (4.88 eV) by itself is not able to do the photodecomposition of ethanol; however, all results shown above allow us to suggest that the photodecomposition is carried out by a nucleophilic attack into the ethanol–water system (hydrogen site 9). The electrons involved in the transfer are from the conduction band of the Ni/C photocatalyst, and they enter into the lowest unoccupied molecular orbital (LUMO) of the ethanol–water system, as shown in Fig. 15.

The photodehydrogenation of the ethanol/water solution is schematized in Fig. 16, and it is described as follows:

First, two atoms of hydrogen are eliminated from $C_2H_5OH_{(l)}$ to form one acetaldehyde molecule (CH_3COH) and one hydrogen molecule:
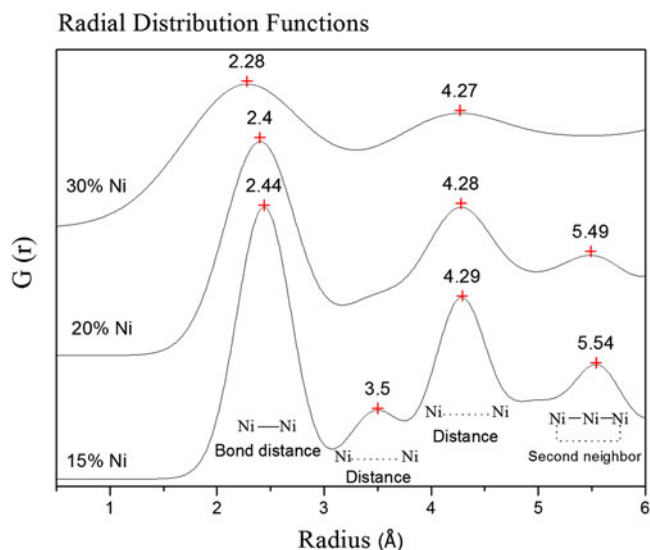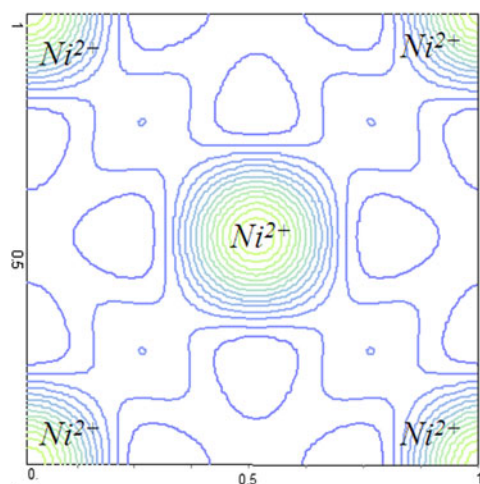

FIG. 9. RDFs obtained by XRD for Ni/C catalysts as a function of Ni content.

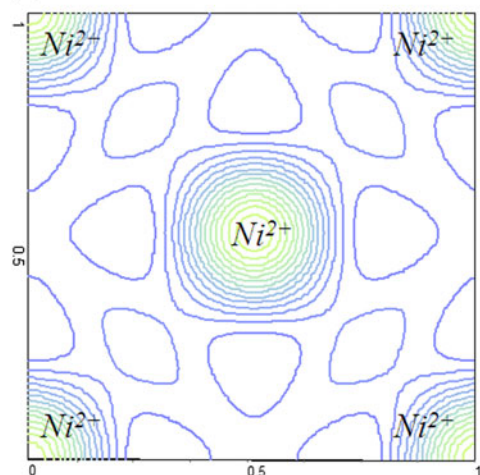TABLE V. RDF peaks of Ni structures for Ni/C catalysts as a function of Ni content.

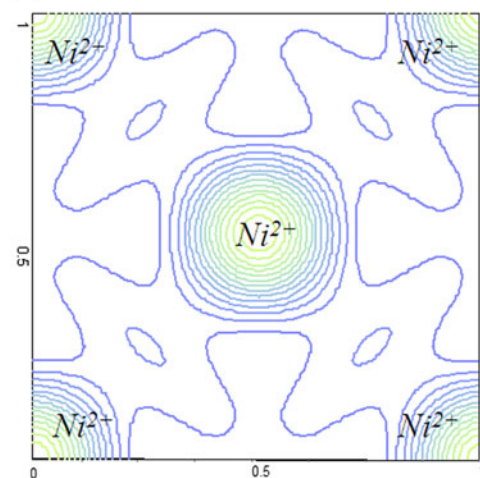| Sample	Interatomic distances (Å)			
	Ni–Ni (first neighbors)	Ni–Ni (first neighbors)	Ni–Ni (first neighbors)	Ni–Ni–Ni (second neighbors)
Ni[a]	2.4917	3.5238	4.3157	4.9834
15% Ni/C[b]	2.4400	3.5000	4.2900	5.5400
20% Ni/C[b]	2.4000	. . .	4.2800	5.4900
30% Ni/C[b]	2.2800	. . .	4.2700	. . .

[a]Theoretical distances.
[b]Obtained by XRD analysis.

FIG. 10. Electron density maps obtained by XRD for Ni/C catalysts: (a) 15%, (b) 20%, and (c) 30% Ni content, respectively.
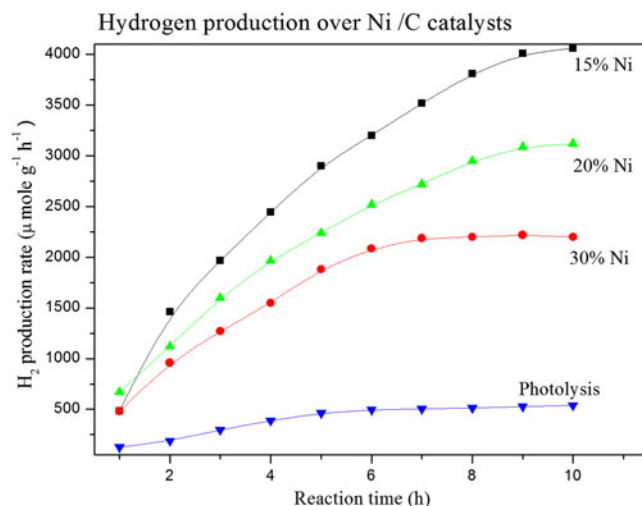

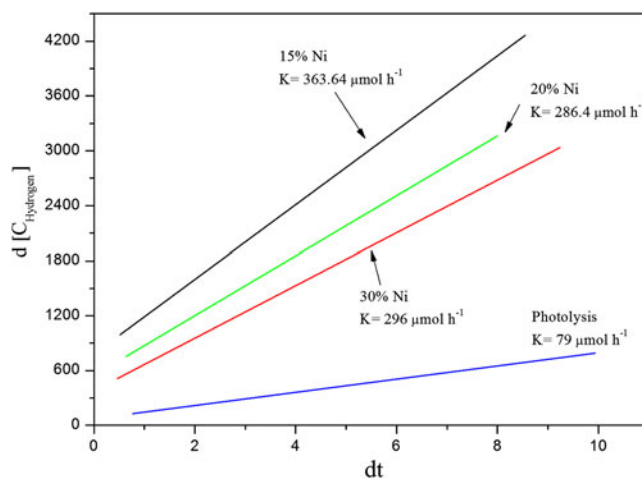FIG. 11. Hydrogen production rate as a function of the reaction time.

FIG. 12. Kinetic constant for the hydrogen production on Ni/C catalysts.
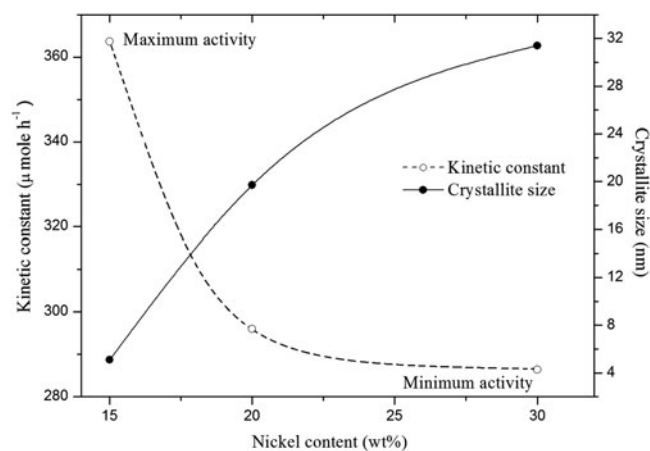

FIG. 13. Kinetic constant and crystallite size as a function of nickel content.
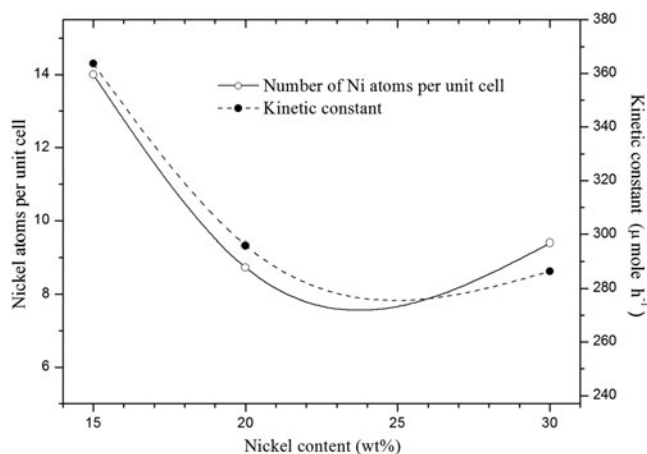
FIG. 14. Whole Ni atoms per unit cell and kinetic constant as a function of nickel content.

TABLE VI. Global molecular properties obtained by DFT/GGA/PBE for ethanol–water and ethanol–ethanol systems.

| System	ΔE (eV)	χ (eV)	η (eV)	E_g (eV)
Ethanol–water	−0.449	2.952	3.655	7.309
Ethanol–ethanol	−0.531	2.629	3.420	6.841

ΔE: interaction energy; χ: electronegativity; η: molecular hardness; and E_g: band gap energy.

TABLE VII. Nucleophilic attack obtained by DFT/GGA/PBE for ethanol–water and ethanol–ethanol systems.

System	Atom[a]	Nucleophilic attack[b]
Ethanol–water	H (9)	0.434
Ethanol–ethanol	H (9)	0.495

[a]See Fig. 15.
[b]It is the highest trend of each system.

$$(1)\quad C_2H_5OH_{(l)} + h\nu \rightarrow CH_3COH_{(l)} + H_{2(g)} \quad .$$
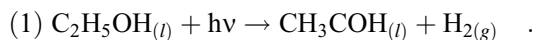
The formation of CH_3CHO molecule as an intermediate was determined by DFT/GGA/PBE calculation, which agrees with Kawai's results,[37] who found by HPLC that the reaction proceeds with intermediate formation of acetaldehyde.

Next, four atoms of hydrogen are eliminated from $CH_3COH_{(l)}$ and two more from $H_2O_{(l)}$ to form three hydrogen molecules:

$$(2)\quad CH_3COH_{(l)} + H_2O_{(l)} + h\nu \rightarrow 2CO_{(g)} + 3H2_{(g)} \quad .$$

In summary,

$$C_2H_5OH_{(l)} + H_2O_{(l)} + h\nu \rightarrow 2CO_{(g)} + 4H_{2(g)},$$
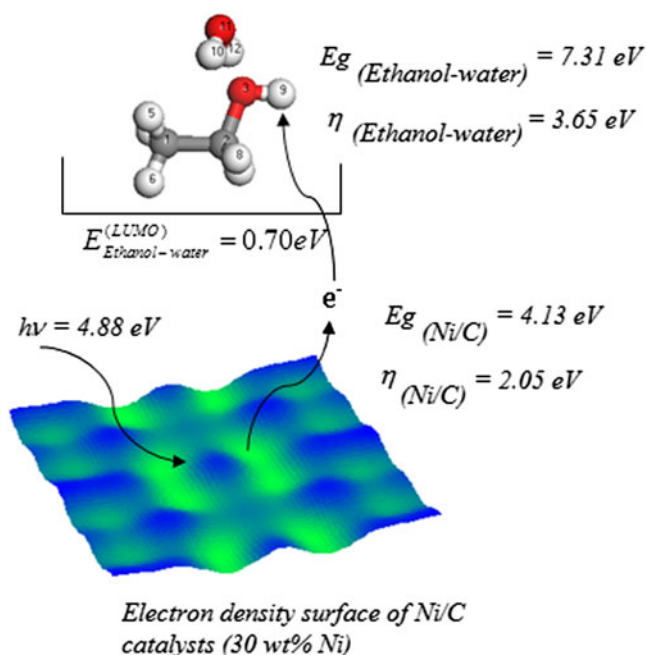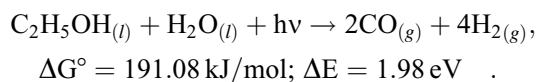$$\Delta G° = 191.08 \, \text{kJ/mol}; \, \Delta E = 1.98 \, \text{eV} \quad .$$
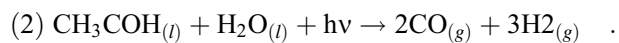
FIG. 15. Nucleophilic attack into the ethanol molecule (hydrogen site 9): electrons involved in the transfer are from the conduction band of the Ni/C photocatalyst, and they enter into the LUMO of the ethanol–water system.
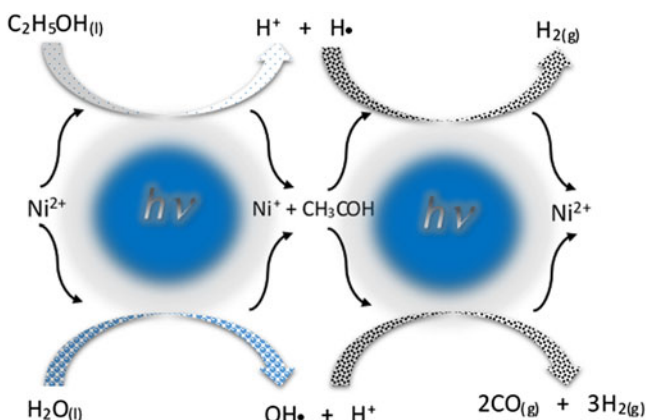

FIG. 16. Photodehydrogenation of the ethanol/water solution over Ni/C photocatalysts.

IV. CONCLUSIONS

The present study shows that increasing Ni content results in a decrease of the surface area, volume intrawall, and volume micropore but leads to an increase in crystallite size in the Ni/C catalysts. It is found that point defects are formed in the nickel structures during annealing, which vary with Ni content. In the sample with 15 wt% Ni, both the number of point defects in Ni structure and Ni crystallite size are the smallest compared to the other two catalysts with high Ni loadings. These important factors greatly affect the catalytic activity for the hydrogen production from the ethanol photodecomposition, which

was confirmed by the reaction that showed sensibility to the crystallite size. A notable relationship between the hydrogen production activity, the crystallite size, and the number of nickel atoms per unit cell in the Ni structure was established.

ACKNOWLEDGMENTS

REFERENCES

1. P. Biswas and D. Kunzru: Steam reforming of ethanol for production of hydrogen over Ni/CeO$_2$–ZrO$_2$ catalyst: Effect of support and metal loading. *Int. J. Hydrogen Energy* **32**, 969 (2007).
2. Y. Zhang, Z. Wang, J. Zhou, J. Liu, and K. Cen: Catalytic decomposition of hydrogen iodide over pre-treated Ni/CeO$_2$ catalysts for hydrogen production in the sulfur–iodine cycle. *Int. J. Hydrogen Energy* **34**, 8792 (2009).
3. Y. Lu, S. Li, L. Guo, and X. Zhang: Hydrogen production by biomass gasification in supercritical water over Ni/γ-Al$_2$O$_3$ and Ni/CeO$_2$-γAl$_2$O$_3$ catalysts. *Int. J. Hydrogen Energy* **35**, 7161 (2010).
4. V.V. Chesnokov and A.S. Chichkan: Production of hydrogen by methane catalytic decomposition over Ni–Cu–Fe/Al$_2$O$_3$ catalyst, hydrogen production by ethanol steam reforming over Cu–Ni supported catalysts. *Int. J. Hydrogen Energy* **34**, 2979 (2009).
5. A.J. Vizcaíno, A. Carrero, and J.A. Calles: Hydrogen production by ethanol steam reforming over Cu–Ni supported catalysts. *Int. J. Hydrogen Energy* **32**, 1450 (2007).
6. A. Venugopal, S.N. Kumar, J. Ashok, D.H. Prasad, V.D. Kumari, K.B.S. Prasad, and M. Subrahmanyam: Hydrogen production by catalytic decomposition of methane over. *Int. J. Hydrogen Energy* **32**, 1782–1788 (2007).
7. Y. Yang, J. Ma, and F. Wu: Production of hydrogen by steam reforming of ethanol over a Ni/ZnO catalyst. *Int. J. Hydrogen Energy* **31**, 877 (2006).
8. M.F.R. Pereira, J.J.M. Órfão, and J.L. Figueiredo: Oxidative dehydrogenation of ethylbenzene on activated carbon catalysts 3. Catalyst deactivation. *App. Catal., A* **218**, 307 (2001).
9. K. Weissermel and H.J. Arpe: *Industrial Organic Chemistry*, 1st ed. (Reverte, Spain, 1981).
10. S. Lowell, J.E. Shields, M.A. Thomas, and M. Thommes: *Characterization of Porous Solids and Powders: Surface Area, Pore Size and density*, 1st ed. (Kluwer Academic Publishers, Netherlands, 2004), pp. 114, 149.
11. P.I. Ravikovitch and A.V. Neimark: Density functional theory of adsorption in spherical cavities and pore size characterization of templated nanoporous silicas with cubic and three-dimensional hexagonal structures. *Langmuir* **18**, 1550 (2002).
12. A.V. Neimark, P.I. Ravikovitch, and A. Vishnyakov: Bridging scales from molecular simulations to classical thermodynamics: Density functional theory of capillary condensation in nanopores. *J. Phys. Condens. Matter* **15**, 347 (2003).
13. M.L. Ojeda, J.M. Esparza, A. Campero, S. Cordero, I. Kornhauser, and F. Rojas: On comparing BJH and NLDFT pore-size distributions determined from N2 sorption on SBA-15 substrata. *Phys. Chem. Chem. Phys.* **5**, 1859 (2003).
14. W.W. Lukens, P. Schmidt-Winkel, D. Zhao, J. Feng, and G.D. Stucky, Evaluating pore sizes in mesoporous materials: A simplified standard adsorption method and a simplified Broekhoff−de Boer method. *Langmuir* **15**, 5403 (1999).
15. V. Mayagoitia, F. Rojas, and I. Kornhauser: Pore network interactions in ascending processes relative to capillary condensation. *J. Chem. Soc. Faraday Trans.* **1**, 2931 (1985).
16. F. Wang and S. Li: Determination of the surface fractal dimension for porous media by capillary condensation. *Ind. Eng. Chem. Res.* **36**, 1598 (1997).
17. A. Neimark: A new approach to the determination of the surface fractal dimension of porous solids. *Physica A* **191**, 258 (1992).
18. R.G. Pearson: *Chemical Hardness. Applications from Molecules to Solids*, 1st ed. (Wiley-VCH, Germany, 1997).
19. R.G. Pearson: Recent advances in the concept of hard and soft acids and bases. *J. Chem. Educ.* **64**, 561 (1987).
20. R.G. Parr and R.G. Pearson: Absolute hardness: Companion parameter to absolute electronegativity. *J. Am. Chem. Soc.* **105**, 7512 (1983).
21. R.G. Pearson: Hard, and soft acids and bases. *J. Am. Chem. Soc.* **85**, 3533 (1963).
22. A. Escobedo Morales, E. Sánchez Mora, and U. Pal: Use of diffuse reflectance spectroscopy for optical characterization of un-supported nanostructures. *Revista Mexicana de Física* **53**, 18 (2007).
23. http://www.esi2.us.es/IMM2/estructuras_cristalinas/estructuras_cristalinas.html.
24. N.H. March: *Electron Density Theory of Atoms and Molecules*, 1st ed. (Academic Press, New York, 1992).
25. M. Magini and A. Cabrini: Programme en FORTRAN IV pour l'analyse des données expérimentales relatives à la diffusion des rayons X par des substances liquides, amorphes et microcristallisées. *J. Appl. Cryst.* **5**, 14 (1972).
26. http://accelrys.com/products/materials-studio/.
27. J.P. Perdew, K. Burke, and M. Ernzerhof: Generalized gradient approximation made simple. *Phys. Rev. Lett.* **77**, 3865 (1996).
28. D.R. Hamann, M. Schlüter, and C. Chiang: Norm-conserving pseudopotentials. *Phys. Rev. Lett.* **43**, 1494 (1979).
29. Y. Zhang, A. Dragan, and C.D. Geddes: Broad wavelength range metal-enhanced fluorescence using nickel nanodeposits. *J. Phys. Chem. C* **113**, 15811 (2009).
30. Z. Shuwen, Y. Xia, L. Wing-Cheung, Z. Yating, H. Rui, D. Xuan-Quyen, H. Ho-Pui, and K-T. Yonga: Size dependence of Au NP-enhanced surface plasmon resonance based on differential phase measurement. *Sens. Actuators, B* **176**, 1128 (2013).
31. H. Comerta and J.N. Pratt: The standard molar Gibbs free energy of formation of NiO from high-temperature e.m.f. measurements. *J. Chem. Thermodyn.* **12**, 1145 (1984).
32. F. Agullo-López, C.R.A. Catlow, and P.D. Townsend: *Point Defects in Materials*, 1st ed. (Academic Press, Waltham, MA, 1988), p. 3.
33. H. Schultz, J. Takamura, M. Doyama, and M. Kiritani: *Point Defects, and Defect Interactions in Metals*, 1st ed. (North-holland, Amsterdam, 1982).
34. R.A. Johnson: Empirical potentials and their use in the calculation of energies of point defects in metals. *J. Phys. F: Met. Phys.* **3**, 295 (1973).
35. C. Kittel: *Introduction to Solid State Physics*, 7th ed. (John Wiley and Sons, Inc., New York, 1996), pp. 541–543.
36. O. Levenspiel: *Chemical Reaction Engineering*, 3rd ed. (Wiley, New Delhi, India, 2007), p. 50.
37. M. Kawai, T. Kawai, S. Naito, and K. Tamaru: The mechanism of photocatalytic reaction over Pt/TiO$_2$: Production of H2 and aldehyde from gaseous alcohol and water. *Chem. Phys. Lett.* **110**, 58 (1984).